Energetic Tin Ions Traversing Hydrogen Gas: SRIM Simulation of Transmitted Ions

University of Groningen

Bachelor Research Project

Applied Physics

Author:
Melav Salih S3484432
Daily supervisor:
S. Rai &
K. Bijlsma

First examiner:
prof. dr. ir. R. Hoekstra
Second examiner:
Dr. T. Schlathölter

July 26, 2020

Abstract

With the minimization of the size of chips in devices, new techniques are needed to provide the next step in the manufacturing process. An important step is the use of EUV light sources. Modern intense EUV light sources for lithography are based on a tin plasma in which highly charged tin ions are the atomic sources of 13.5 nm EUV light. However, high energy tin ions coming from the plasma can damage the collector mirror inside the source chamber. Hydrogen gas under low pressures is used to reduce the impact. This thesis provides insight into the stopping powers and ranges of tin ions, with energies of 0.1 keV, 1 keV, and 10 keV, in hydrogen gas using simulations with the program package SRIM. Furthermore, the angle of transmitted ions and energy spectrum are plotted over different target depths of hydrogen gas to observe the scattering angle and their respective shifts in the energy spectrum.

Contents

1 Introduction

The most relevant law in modern microchips technology that stimulates the growth of the industry is Moore's Law which was postulated by the co-founder of Intel, Gordon E. Moore, in 1965. This law predicts the number of microchips on a transistor doubles while the production of such devices grows cheaper every couple of years. In the past few decades, this has proven to be true as the technological impacts continue to grow exponentially [1]. To make chips, a process called lithography is used; concentrated beams of photons with short wavelength and thus high energy produce a pattern onto a semiconductor wafer on which the circuit is etched onto to produce the chip. Using typical forms of lithography such as optical nanolithography and photo-lithography at the nano-scale with a wavelength of 193 nm enabled chip manufacturers to reduce the dimension to less than20 nm. The very short wavelength at the nano and micro-scale allows for very high-precision structure manipulation, ensuring high transistor density chips. However, to continue the trend, systems with shorter wavelengths are required. Samsung and Intel, for example, have been neck-in-neck the past few years challenging their own compact devices, investing hundreds of millions of dollars into manufacturing systems that companies, such as ASML, produce. With the global technological developments and persistent necessity for several industries to acquire affordable advanced devices and sensors, it is only natural for businesses to invest more stocks into ASML with its cutting edge of the chip fabrication machinery.

Currently, ASML is the first and only producer of deep ultraviolet (DUV) and extremely ultraviolet (EUV) lithography machines [2]. EUV light has a wavelength of 13.5 nm making it 14 times smaller than DUV light enabling the continuing trend of Moore's Law. A laser is shot at a tin droplet target which expands into a hot-dense plasma of tin ions which emit the EUV light that is then collected with a hemispherical mirror [3]. The placement of the multilayer mirrors of molybdenum (Mo) and silicon (Si) results in the EUV light being focused into the nanolithography machine.

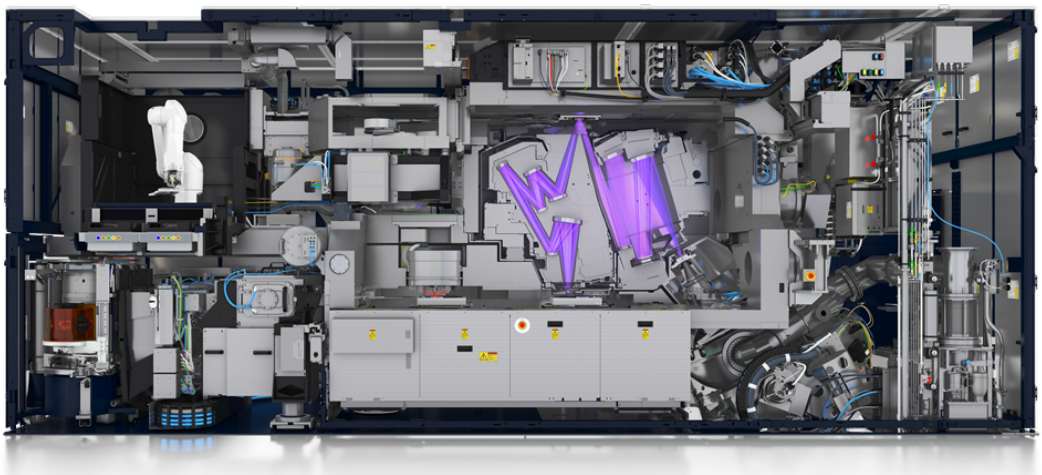

Figure 1.1: An EUV lithography machine as seen from the inside. *Image adapted from [2].*

Consequently, energetic tin ions can damage the mirrors as they charge forth in a bullet-like manner as corpuscular debris produced from the sources. This is a big challenge in EUV systems. Three gases were considered to be possible solutions in the specific pressure level and effectiveness: argon (Ar), helium (He), and hydrogen (H_2) [4]. The solution that ASML found to be best is the injection of hydrogen gas through the vacuum chamber to mitigate the high influx of tin debris by reducing its energy. Through multiple collisions, the momentum is exchanged which slows down the energetic tin ions and redirects it toward the vacuum exhaust [5].

However, the knowledge behind the interaction between tin ions and hydrogen molecules is lacking. This research studies transmitted tin ions going through different target depths of molecular hydrogen using SRIM (The Stopping and Range of Ions in Matter [6]) package simulations for energies between 0.1 keV and 10 keV.

2 Theory

This section discusses the relevant theory with the focus on heavy ions in a light target. In section 2.1 the interactions of ions with matter are explained including scattering, the over-the-barrier model, single electron capture, and the molecular hydrogen energy levels. Next, the stopping power is explained in section 2.2 by subdividing it into electronic stopping and nuclear stopping. Finally, SRIM is described in length in section 2.3 to look into the approximations made computationally, the phase correction and compound correction that the program implements.

2.1 Interactions of ions with matter

Several different types of interactions occur when an ion beam hits a target. For example, electron or photon emission, electron transfer, scattering, adsorption, and sputtering; each interaction has its own unique cross-section. The focus of this thesis will be the scattering event where the effects of thermal vibrations, phonon oscillations and interatomic binding are ignored [7]. The energy needed to ionize hydrogen is around 16 eV, hence in the high-keV range secondary electrons may be produced [8].

2.1.1 Scattering

When particles collide with each other and deviate from their straight trajectories, scattering occurs. This can be either elastic or inelastic scattering. In elastic scattering, no energy is absorbed by either particle during the collision. On the other hand, in inelastic scattering, one or both of the particles involved in the collision absorb some or all of the original kinetic energy. For the remainder of this thesis, the focus will be on Rutherford elastic scattering as shown in equation 10 and further expanded in section 2.2.2. As tin ions are far heavier than the hydrogen molecule, there is no backscattering. Rather, they are all scattered in the positive direction as a result of collisions; hence, the ions are transmitted through the target.

Binary elastic collision, the most general form, is when two particles collide to perform a single collision where the energy is transferred from the projectile to the particle. This energy loss depends on the masses of the particles. Since the mass of tin is significantly larger than that of hydrogen gas, the lost energy is very small. The conservation of energy and momentum, in the x- and y-direction, are formulated below:

$$\frac{1}{2}m_p v_0^2 = \frac{1}{2}m_t v_t^2 + \frac{1}{2}m_p v_p^2 \tag{1}$$

$$m_p v_0 = m_t v_t \cos\theta + m_p v_p \cos\phi \tag{2}$$

$$m_p v_p \sin\theta = m_t v_t \sin\phi \tag{3}$$

where m_p and m_t are the masses of the projectile (ion) and target, respectively and v_0, v_t, v_p are the velocities representing the initial velocity of the projectile and the final velocities of the target and projectile, respectively. The angle θ is the scattering angle while angle ϕ is the recoil angle.

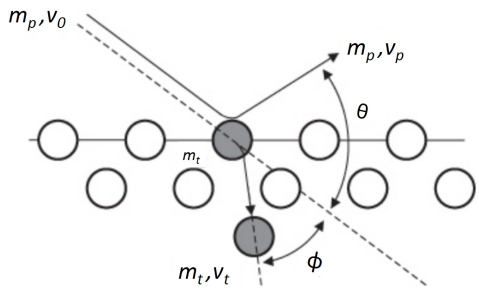

Figure 2.1: The binary collision model: the collision of a projectile atom with a target atom resulting in a scattered ion or recoil atom. Adapted from [9].

2.2 Stopping power

As an ion moves through a target of a certain depth, it loses its energy to the target through different processes which will be explained below. The *inelastic energy loss*, called the *stopping power* and denoted by dE/dx in this thesis, is defined as equation 4.

$$\frac{dE}{dx} = -n \cdot S(E), \tag{4}$$

dE is the energy loss of the ions moving through a gas layer with particle density n and dx is the target depth or thickness of the gas. The atomic stopping cross section $S(E)$ has two components: *nuclear stopping* S_n and *electronic stopping* S_e. For tin, the nuclear stopping power has a maximum at projectile energies of the order 100-1000 keV, while for the electronic stopping power this is of the order 100-1000 MeV [6]. Therefore, the former is dominant in this research and the electronic stopping power effect can be neglected. This is clearly shown in figure 2.2 using calculations from SRIM.

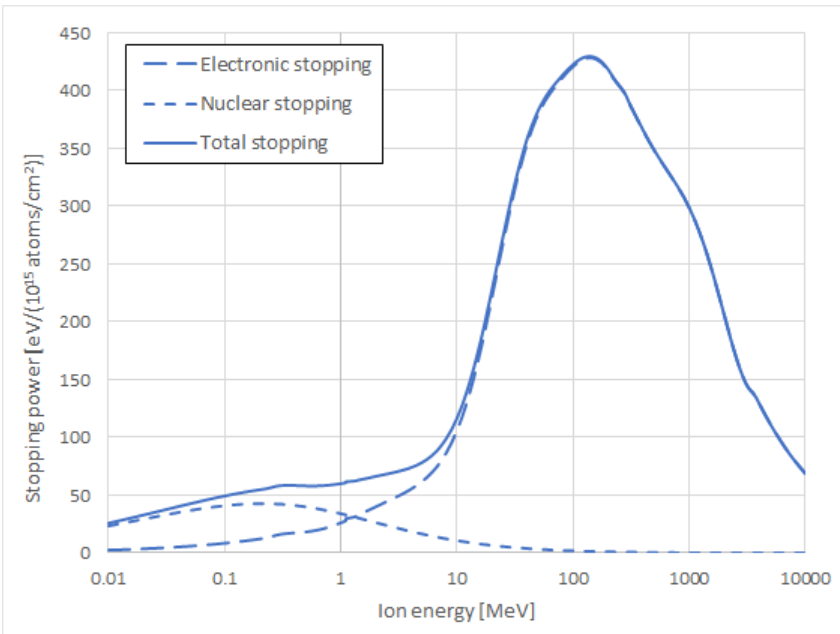

Figure 2.2: Stopping powers of tin ion in hydrogen gas target from 0.01 MeV to 10 000 MeV from the stopping/range tables in the SRIM package. The effect of the electronic stopping power is equal to that of the nuclear stopping power at about 1 MeV. The Bragg peak is at around 100 MeV.

2.2.1 Electronic stopping

Electronic stopping is the process where an energetic ion continuously loses its energy to the electrons of the target atom [6]. This can be caused by different processes, such as electron-electron collisions, excitation or ionization of target atoms and ionization of conduction electrons. The electrons in a target can go through inelastic collisions with a projectile and be ionized or excited.

The electronic stopping power is explained using the non-relativistic Bethe-Bloch equation [10]:

$$-\frac{dE}{dx} = n \cdot S_e(v) \text{ [eV/m]}, \tag{5}$$

where n is the number density of scattering centers and $S(v)$ is the stopping cross section as a function of the velocity of the ion.

$$S_e(v) = \frac{4\pi e^4 Z^2}{mv^2} \ln \frac{2mv^2}{I} \text{ [eV m}^2\text{]}, \tag{6}$$

where e and m are the charge and mass of the electron, Z is the charge of the ion, and I is the mean excitation potential of the target. From the relation, it is clear that the electronic stopping energy depends on the constantly changing ion velocity as the ion penetrates the target and is stripped of some of its electrons resulting in its charge state becoming a function of the target.

However, for low velocities below the electronic stopping maximum which will be the focus of this thesis, the Lindhard and Scharff velocity dependent relation (equation 7) is used for the electronic power for $v < v_1 = v_0 \cdot Z_1^{2/3}$ [11].

$$S_e = \zeta_e \cdot 8\pi e^2 a_0 \cdot \frac{Z_t Z_p}{Z} \cdot \frac{v}{v_0}, \tag{7}$$

where a_0 is Bohr's radius, $\zeta_e \approx Z_1^{1/6}$, $Z = (Z_1^{2/3} + Z_2^{2/3})^{3/2}$, v is the velocity of the ion, and $v_0 = e^2/\hbar$. This holds true with little error for very low velocities below 10 keV/u.

2.2.2 Nuclear stopping

Unlike the electronic stopping energy, the nuclear stopping energy is in discrete amounts. Nuclear stopping is dependent on the Coulomb repulsion between the nuclear charges of the atoms. This includes all the processes in which the energy of the ion as a whole is transferred to the target through elastic collisions. The Coulomb potential, U, is given by equation 8:

$$U = \frac{Z_p Z_t}{r} \text{ [a.u.]}, \tag{8}$$

where Z_p and Z_t are the nuclear charge states of the projectile and target atom, respectively, and r is the inter-nuclear distance. Ziegler, Biersack and Littmark proposed a screening function $\Phi(\frac{r}{a})$ to construct the ZBL potential, shown in equation 9, obtained by fitting the universal potential function to a number of theoretically calculated interatomic potentials [6]. This equation was derived from Rutherford's elastic scattering (also known as Coulomb scattering) as shown in equation 10.

$$V(r)^{ZBL} = \frac{Z_p Z_t e^2}{4\pi\epsilon_0 r} \cdot \Phi\left(\frac{r}{a}\right) \tag{9}$$

where $\Phi\left(\frac{r}{a}\right) = 0.1818e^{-3.2r/a} + 0.5099e^{-0.9423r/a} + 0.2802e^{-0.4028r/a} + 0.281e^{-0.2016r/a}$ and a is the Thomas Fermi screening radius of the collision, $\frac{0.8853}{Z_p^{0.23}+Z_t^{0.23}}$. Without the screening function in the center-of-mass coordinate system, the Coulomb scattering formula for differential cross-section $d\sigma/d\Omega$ is

simplified to equation 10 which is derived from the conservation equations 1 to 3 [12].

$$\frac{d\sigma}{d\Omega} = \left(\frac{Z_p Z_t e^2}{4E_0 \sin^2 \frac{\theta}{2}} \right)^2 \tag{10}$$

where E_0 is the initial kinetic energy of the ion and θ is the deflection angle.

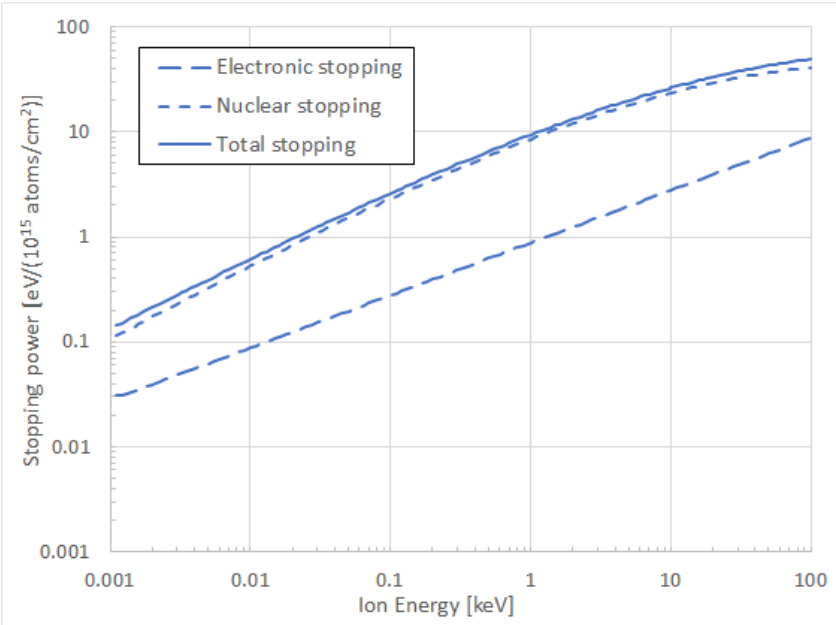

Figure 2.3: Stopping powers of tin ion in hydrogen gas target from 0.001 keV to 100 keV from the stopping/range tables in the SRIM package. The electronic stopping power is nearly negligible in comparison to the nuclear stopping power in the low velocity region. There is a near-linear relation on the double logarithmic scale between the ion energy and the stopping powers.

2.3 SRIM

The Stopping and Ranges of Ions in Matter developed by James F. Ziegler is a collection of programs that use a Monte Carlo method to simulate ion-target interactions. The impact parameters, defined as the distance at which the particles would pass each other if no forces acted between them, of every ion are varied slightly to produce different outcomes to simulate a beam of ions hitting a solid (or gas) target. Despite all the approximations that will be explained below, the average error of the simulations is 2% with exceptions of 5% for heavy ions in light targets; this is due to a lack of experimentally data to correct the calculations used in the program [6].

2.3.1 Approximations and assumptions

After multiple approximations, the SRIM software's computation time is significantly reduced. For the purpose of accurate analysis, these must be noted. First, the Monte Carlo method in use is the binary collision approximation where the ion is assumed to move through the target by experiencing a series of elastic collisions with the atoms in the material always resulting in subsequent straight lines, losing its energy to the target electrons through electronic stopping power [6]. The target is assumed to be fully amorphous making the distance between each collision equal to $N^{-1/3}$ where N is the atomic density of the material. However, the interactions with the nuclei are ignored. To calculate the scattering angle and energy loss of a binary collision a so-called collision integral is evaluated. A collision integral

is a complex mathematically constructed equation to describe particle collisions based in inter-atomic potentials [13].

Furthermore, in a solid target, ions will get implanted and the surface constantly undergoes changes throughout the collision experiment. However, SRIM does not track such changes as it assumes a static target. As the initial position of the projectile ion is below the first monolayer of the target, it is impossible to observe a single backscattering peak when the scattering angle is less than twice the target angle [14]. Since here a gas target will be used and tin is much heavier than hydrogen, this will not be an issue.

Most importantly, SRIM takes STP (0 °C, 760 mm) conditions making it increasingly difficult to simulate this experiment for very low pressures. This will be further elaborated in the experimental setup in section 3.2.

2.3.2 Energy straggling

The distribution of energy loss about an average value is called *straggling* and is described in SRIM as a series of moments [6]. The units of energy straggling are [(energy loss)^2 / distance]. By analytically comparing the most relevant theories, the equations used in TRIM are explained below. However, the target surface roughness and changes in the charge state of the ion as it moves through the target are not considered in SRIM [6]. Just as it affects the stopping power, this also affects the straggling. Similar to the stopping power, energy straggling is divided into electronic and nuclear straggling.

The origin of particle straggling comes from the derivation of Bohr straggling, which is the straggling between a moving charged particle and a stationary charged particle, in the limit of non-relativistic Coulomb interactions. Equation 11 gives the classical Bohr straggling formula for the two-particle collision where T is the energy loss to the stationary particle, which varies with the impact parameter. By integrating over all impact parameters, one may obtain the mean of the energy-loss squared. $< T^2 >\equiv \int_0^\infty T^2 d\sigma)/\sigma$, where σ is the geometric cross-section, defined as $d\sigma = 2\pi p dp$, with p being the impact parameter [6]:

$$Q_2 \equiv < T^2 > / < \Delta x >= \pi\gamma Z_p^2 e^4 M_p/(< \Delta x > M_t\sigma), \tag{11}$$

where Δx is the distance traveled by the projectile and $\gamma \equiv 4M_1M_2/(M_1 + M_2)^2$.

Electronic straggling

By approximating this for the energy loss between an ion and an electron, the final equation 12 is derived, the Bohr electronic straggling [15] for ion energies greater than 25 keV/u:

$$Q_2 = 4\pi e^4 Z_1^2 Z_2 N \Delta x, \tag{12}$$

where N is the atomic density of the target [atoms/cm^3].

For lower ion energies, as used in this thesis, the TRIM program (Section 3.2) uses the Firsov straggling. His prediction stated that at low velocities, the straggling is approximately proportional to the projectile energy up to the Bohr value [16]. This is further elaborated below in the nuclear straggling.

Nuclear straggling

Similar to the stopping power's dependence on nuclear stopping in low velocity regions, the energy straggling is also predominantly nuclear straggling. To derive the nuclear straggling, a set of formulas

were analytically compared for the pure Coulomb interaction with the exact data for realistically screened potential to fit the curves to a good approximation with less than 9% relative error [16]. The equation 13 includes the screened interaction:

$$W_2 = \frac{1}{4 + 0.197\varepsilon_1 + 6.584\varepsilon_2} \tag{13}$$

where $\varepsilon_1 = \varepsilon^{-1.6991}$ and $\varepsilon_2 = \varepsilon^{-1.0494}$. The unit for nuclear straggling is dimensionless.

2.3.3 Projected range and straggling

Before diving into the details of projected range and straggling, it is important to note that in TRIM, to increase efficiency, all collisions which transfer negligible amounts of energy and cause negligible deflection angles in the ion trajectory are scaled together. The definition of "negligible" is assumed in TRIM to be any random quantity (non-cumulative) which has less than 0.1% effect of the final results [6].

The projected range of an ion is defined as the sum of the ion ranges divided by the number of ions to give a mean value. The simplified range formula is obtained through the integration of the stopping power dE/dx which ignores the energy straggling effects [11]. This is given in the longitudinal direction, the lateral direction, and the radial direction in which cylindrical symmetry of the ion distribution is assumed which is further shown in figure 2.4.

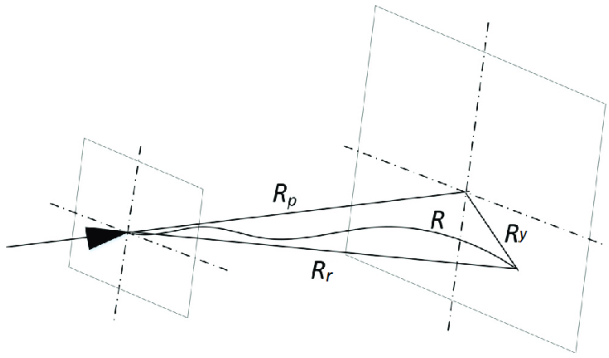

Figure 2.4: Illustration of the range straggling in the three different distribution, R_p, R_r, R_y. Sketch adapted from [11].

Range straggling is directly related to the ion velocity at low energy [16]. This is given by equation 14:

$$< \Delta p^2 >= \gamma \cdot \int_0^{\epsilon} \frac{W(\epsilon')d\epsilon'}{[S_n(\epsilon') + S_e(\epsilon')]^3} \tag{14}$$

where $\epsilon = aM_tE/Z_pZ_te^2(M_p + M_t)$ is the reduced energy; S_n and S_e are the nuclear and electronic stopping power, respectively.

Straggling is the square root of the variance where range straggling is defined for the three different distributions [6]. The equation 15 is summarised from equation 14 above:

$$\text{Straggling } \equiv \sigma = [(\sum_i x_i^2)/N - R_p^2]^{1/2} \qquad =< (\Delta x_i)^2 >^{1/2} \tag{15}$$

$$\text{Radial straggling } \equiv \sigma_r = [(\sum_i (y_i^2 + z_i^2)/N - R_r^2]^{1/2} \qquad =< (\Delta r_i)^2 >^{1/2} \tag{16}$$

$$\text{Lateral straggling } \equiv \sigma_y = [(\sum_i ((|y_i| + |z_i|)/2)^2)/N]^{1/2} \tag{17}$$

In lateral straggling, the mean lateral projected range is zero (i.e. $R_y = 0$) due to the assumption that cylindrical symmetry of the range distribution exists for a normally incident beam. The dimensions of both the projected range and straggling is length.

Magic formula

Biersack's Magic Formula allows for quick solution (up to 50x over other methods) of the scattering problem with high precision [17]. It is an analytic formula for the evaluation of atom-atom scattering.

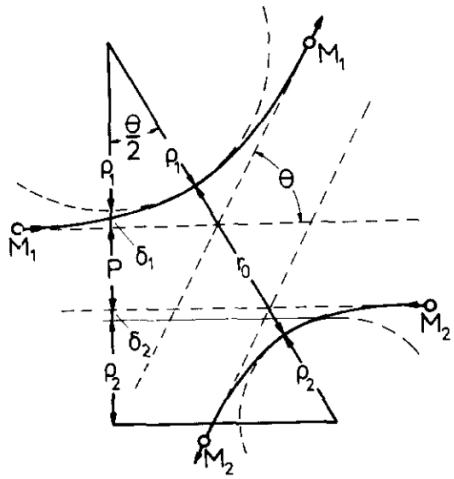

Figure 2.5: *A graphical representation of the particle trajectories in the center of mass system with the superimposed "scattering triangle," comprised of the impact parameter p, radii of curvature* ρ_1 *and* ρ_2*, distance of closest approach* r_o*, and the correction terms* δ_1 *and* δ_2*. From this construction* $\cos\theta/2$ *is obtained in the Magic formula [17].*

$$\cos\frac{\theta}{2} = \frac{\rho + p + \delta}{\rho + r_0}, \text{with } \rho \equiv \rho_1 + \rho_2 \text{ and } \delta \equiv \delta_1 + \delta_2 \tag{18}$$

By expressing the length in units of the screening length a, the definition of the Magic Formula is derived in equation 19.

$$\cos\frac{\theta}{2} = \frac{B + R_c + \Delta}{R_0 + R_c}, \tag{19}$$

where $B = \frac{p}{a}$, $R_0 = \frac{r_0}{a}$, $R_c = \frac{\rho}{a}$ and $\Delta = \frac{\delta}{a}$. The Magic Formula is used for determining the scattering angle of both the ion and the recoil, and also the transferred energy during the collision.

Deflection angle

The projectile's outgoing angle α, with respect to the normal to the target surface, for one collision is given in equation 20. The directional cosines with respect to the other Cartesian coordinates (Y and Z) are derived similarly for following the particle trajectories in three-dimensional space [6]:

$$\cos\alpha_1 = \cos\alpha_0 \cos\theta_1 + \sin\alpha_0 \sin\theta_1 \cos\phi_1 \tag{20}$$

where α_0 is the incidence angle inputted by the user and θ is the laboratory scattering angle; and $\phi = 2\pi R_n$ is the azimuthal scattering angle which is randomly selected through R_n as it is uniformly distributed between 0 and 1.

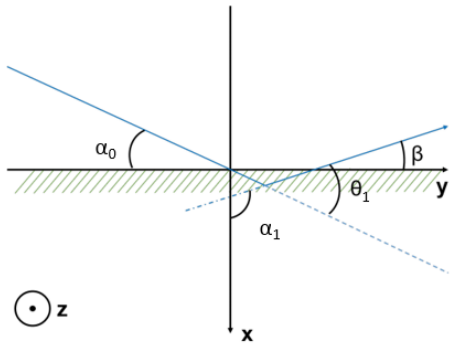

Figure 2.6: Schematic of a scattered projectile ion in blue with its angles as described by SRIM. Adapted from [3].

2.3.4 Phase correction

As solids and gases behave differently in their structures, a correction was introduced by SRIM. One of the biggest challenges of stopping theory is calculating this correction theoretically [6]. In a solid, electrons may form a continuous cloud of mobile conduction electrons which can interact with the ion collectively, giving more collisions. This implements a correction factor for the ion's charge state which is lower in the gas phase due to less collisions and more space. Second, an ion will interact with successive atoms very quickly and excitations of its own electrons may not relax before a subsequent collision, increasing the local target electron density around the ion. However, due to the decreased electron density of a gas, the correction lowers the density of the ion-electron interactions. Lastly, the ion's polarization of a target electron will shield the ion from having distant collisions as an effect of the above. Consequently, the gas phase has more interactions with these distant electrons.

The first and second correction increases the stopping power of the material in the gas phase while the third decreases the stopping power. As a result of all the corrections, the stopping of ions is higher in a gas target than in a solid target when measured by transmitting the same number of atoms/cm^2. The phase correction disappears at 2 MeV/u but makes up to two times the change in stopping powers in low velocities [6].

2.3.5 Compound correction

In addition to the phase correction, SRIM accounts for compound corrections as well. This is simply because bonded atoms behave differently from independent atoms due to shared electrons and/or orbitals. Atomic bonding has large effects on the stopping powers of simple molecules. Bragg's rule estimates the stopping of a compound by the linear combination of the stopping powers of individual elements [18]; however, this gives several limitations. Firstly, the energy loss to the electrons in a material depends on the detailed orbital and excitation structure of the matter. Hence, any differences between elemental materials and the same atoms in compounds will cause a deviation from the rule. Moreover, any bonding changes may also alter the charge state of the ion, changing the strength of its interaction with the target medium.

In 1983, the Core and Bond (CAB) method was proposed where 162 different experiments for light ions were used for calculating the corrections necessary [19]. Stopping powers in compounds can be predicted by using the superposition of stopping by atomic "cores" and then adding the electronic stopping due to the bonding electrons. By investigating the chemical bonds, it was found that they contain the necessary correction. In our case for H_2, for protons at 125 keV in [eV/(10^{55} atoms/cm^2)], as shown in table

1. Since the hydrogen atom only has one electron which is included in the atomic bond, there is no contribution to the atomic "core". The value found for the stopping due to the atomic "bond" is in relation to the electronic stopping only as further shown in figure 4.1 in the results.

Table 1: CORE and BOND stopping values for H_2 adapted from table 5-1 in [6]

Stopping due to atomic:		Stopping power
CORES	Target atom H	0.000
BONDS	Hydrogen bond H-H	9.590

Light atoms have the largest bonding effect on the stopping power which is evident as the correction term for H_2 is 1.35 resulting in a 35% increase in stopping for ion energies around the peak (100 MeV/u). The effects of these deviations on the simulations used in this thesis will be further shown in the results.

3 Experimental Setup

As the research presented in this thesis was done through simulations rather than experiments, the setup of the simulations will be detailed in this section. An example of the ion trajectory in the simulation is shown in figure 3.4. Furthermore, the inputs and outputs of SRIM are explained with visuals in section 3.2.

3.1 Ion beam

The source used in SRIM emits a single energy ion beam which interacts with the target atoms. In this thesis, the energies used for the ion beam are 0.1 keV, 1 keV, and 10 keV.

3.2 SRIM

3.2.1 Ion stopping and range tables

To computationally evaluate the stopping powers of tin ions with different energies, the ion stopping and range tables program in SRIM was used as shown in figure 3.1.

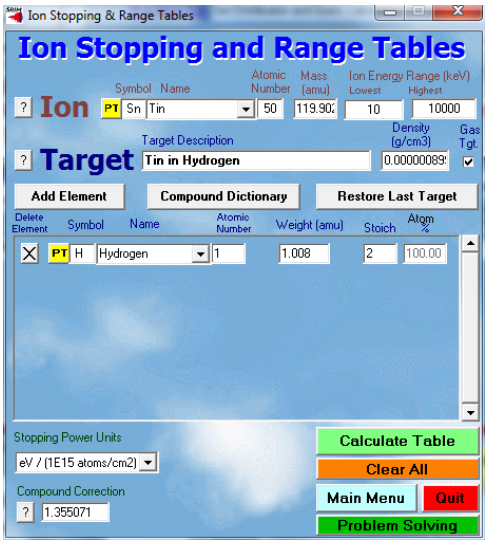

Figure 3.1: The starting window in SRIM to calculate the stopping powers with different ranges.

As there is a significant difference in the density between a gas and solid, it is crucial to evaluate the stopping powers independent of the density, hence the mass stopping power rather than the linear stopping power. SRIM allows for the calculation of both depending on the unit. The stopping power unit shown in figure 3.1, eV/(10^{15}atoms/cm^2), is not only independent of density, but also of mass, hence gives the most accuracy when comparing the correction factors shown in figure 4.1.

3.2.2 Transport of Ions in Matter - inputs

In figure 3.2, the opening window of TRIM calculations is shown. All the inputs that are consistently used throughout this thesis will be explained in this section.

As this thesis studies the effect of a heavy ion on a light gas target, the type of damage calculation used in SRIM is "Ion Distribution and Quick Calculation of Damage". This ignores the target atom cascades and limits the calculation the ion trajectories [6]. As there is no sputtering and our main interest lies in the final distribution of the ions in the target, the energy loss by the ion into the target and the transmitted ions, this will give the same results as the other damage calculations presented with a shorter computational time. To further increase the calculation speed of TRIM, "NO Graphics" is chosen for basic plots as the pattern is more or less the same for the different simulations presented in the results.

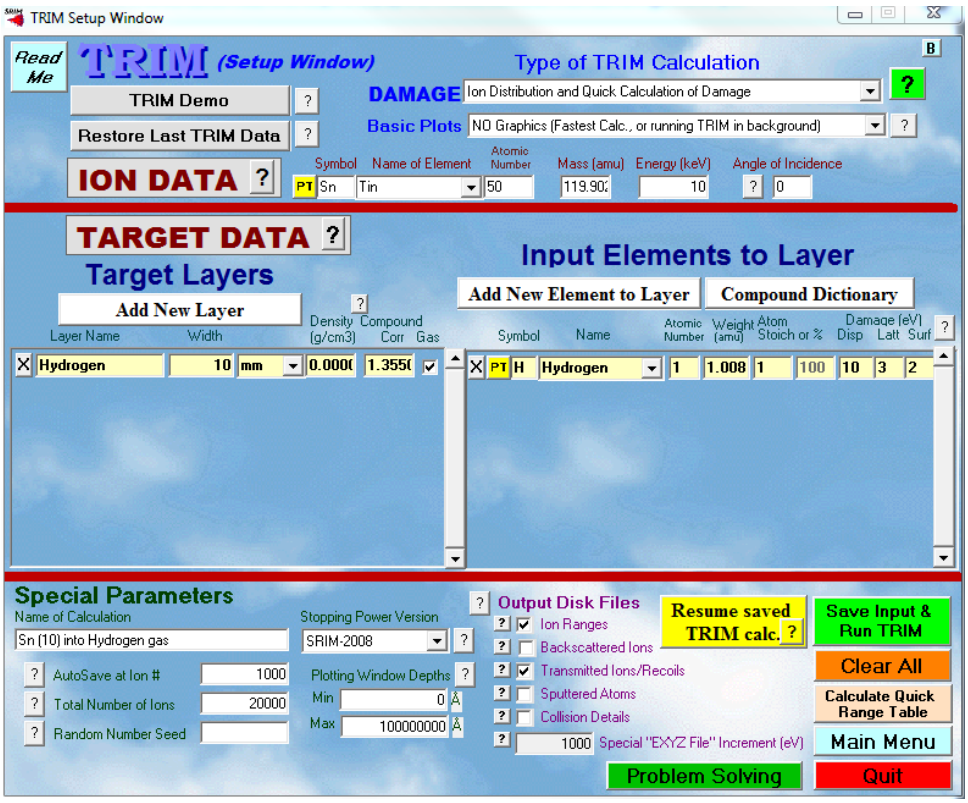

Figure 3.2: TRIM Setup Window as used for 10 keV Sn ions in 10 mm of H_2 target with a density of $\rho = 8.9900 \times 10^{-7}\,\mathrm{g\,cm^{-3}}$ in TRIM.

The angle of incidence is defined with respect to the target surface. Along the X-axis is defined to be 0° as the ion is usually perpendicular to the target surface. This is the case in this research.

The Compound Dictionary includes hydrogen gas with its phase correction and compound correction as explained in section 2.3. The binding energies (displacement energy, surface binding energy, and lattice

binding energy) of the target atoms values are left as defaults. In solids, these values are used to calculate the damage events in eV.

It is important to note that the density used is directly proportional to the pressure. As SRIM uses STP conditions, the density given is for a pressure of 1 bar. The parameters this thesis would like to focus on should be equivalent to that of a target depth of 1 cm at a very low pressure of 10×10^{-5} mbar. When thinking about the volume of this target depth, one can alter two things: the density and the depth. The density is directly proportional to the pressure; therefore, reducing the density by two orders of magnitude, would lower the pressure down to 10 mbar. The density could not be reduced any further as SRIM would round down to 0. Pressure is also directly proportional to the target depth; by reducing the target depth, the volume that the particles are contained in also decreases. Therefore, a target depth of 1 µm would make up for the high pressure, theoretically giving the same number of particles as in a target depth of 1 cm at a very low pressure of 10×10^{-5} mbar.

Furthermore, selecting any of the OUTPUT DISK FILES will save a file in `.txt` in the SRIM Outputs folder with the inputs displayed at the header of the file. They can also be turned On/Off in during the calculation in the output window (see figure 3.3). The output file of interest in the following thesis is "Transmitted Ions".

3.2.3 Transport of Ions in Matter - outputs

In figure 3.3, the window after pressing "Save Input & Run TRIM" from figure 3.2 is displayed. Here the outputs can be summarised and altered.

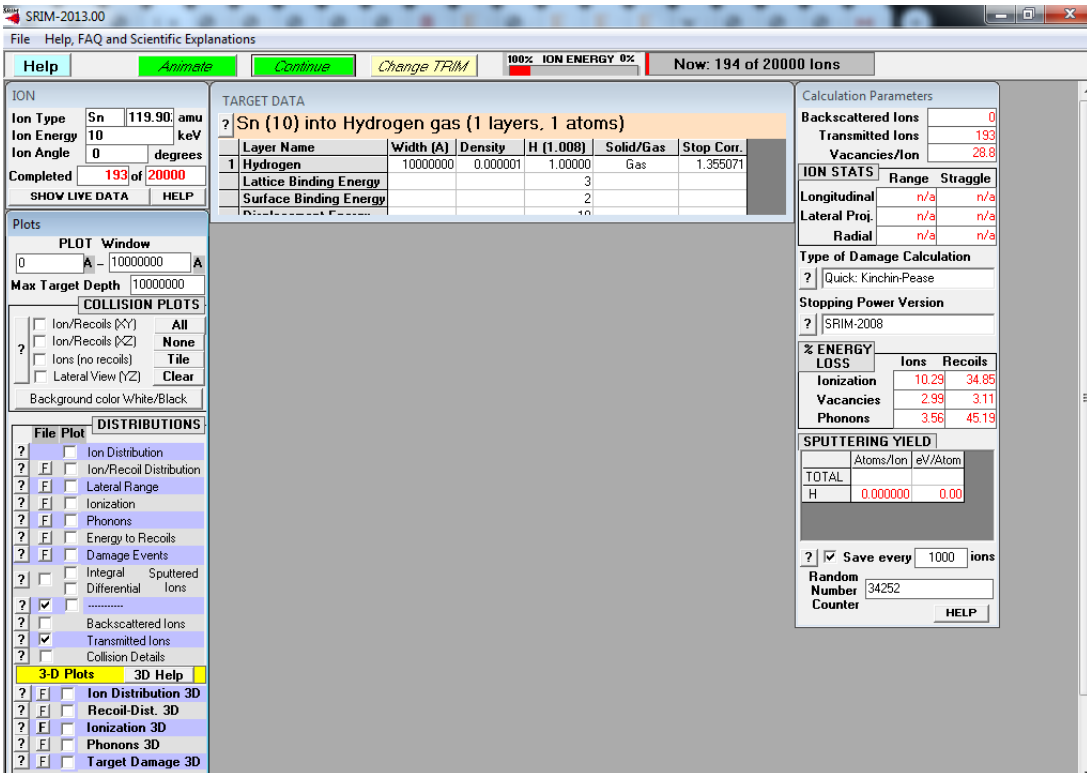

Figure 3.3: TRIM running Window for 10 keV Sn ions in 10 mm of H_2 target with a density of $\rho = 8.9900 \times 10^{-7}\,\mathrm{g\,cm^{-3}}$. Since all the ions are transmitted, there are no IONS STATS. From TRIM.

Despite figure 3.3 missing IONS STATS, these values are very important in the evaluation of the stopping powers for different ion energies. The range and straggle of the longitudinal, lateral and radial projection

are displayed in this table which give an indication of how far the ions are projected. Furthermore, as explained in section 2.3, this is directly related to the velocity which is related to the stopping power. It is crucial to understand the ion distribution within the target depth. The longitudinal range and straggle are in the x-direction, hence with respect to the target depth. The lateral projection is the average final y-z displacement and the radial straggle is the mean radial displacement from the x-axis assuming cylindrical symmetry.

In the "TARGET DATA" window, the target values are displayed which are also included in any PLOT file output. As stated in the inputs, these values are kept as defaults. The "COLLISION PLOTS" show the different trajectories as in figure 3.4.

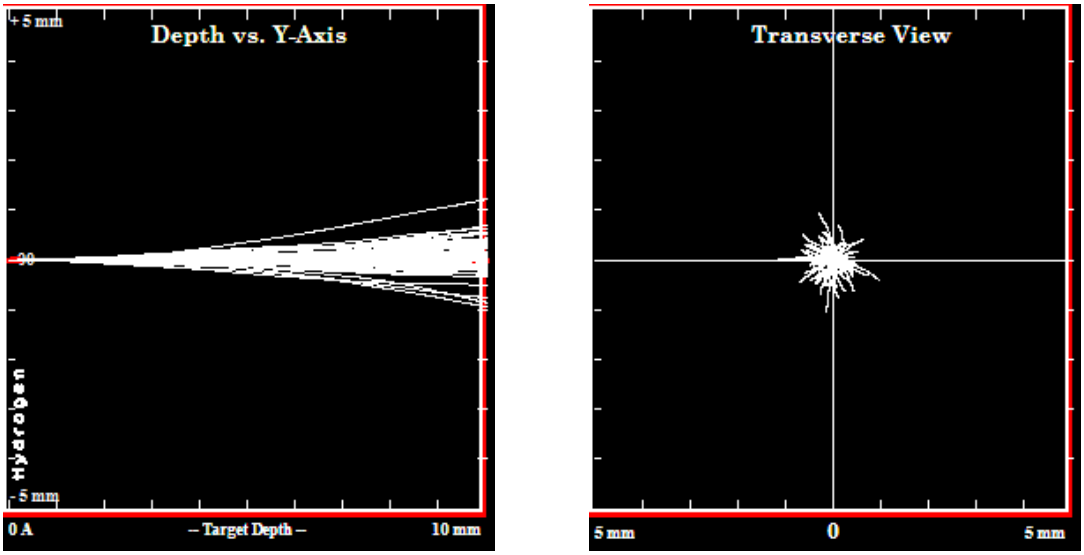

Figure 3.4: An example of the trajectories of 10 keV Sn ions in 10 mm of H_2 target with a density of $\rho = 8.9900 \times 10^{-7}\,\mathrm{g\,cm^{-3}}$. On the left, the longitudinal trajectory in the XY plane where X is the target depth and the direction of the ion beamline and Y is the perpendicular axis. The spread along the beamline is the straggling. On the right, the lateral trajectory in the YZ plane. This depicts a ring-like deviation from the beamline in the transverse view. Image generated from SRIM.

Most of the plots shown in "DISTRIBUTIONS" are irrelevant for transmitted ions. Only the Ionization, and Energy to Recoils plots can be displayed. Energy Loss to Ionization summarises the energy loss to the target electrons within the target window directly from the ions and recoiling atoms. EEnergy Loss to Recoil Atoms shows the direct energy loss by the ion to the various target atoms. This energy loss, plus the direct energy loss of the ion to the target electrons, sum to the energy loss of the ion into the target. Each of the above plots also includes a `.txt` file as an output which can be used in MatLAB to further be analysed. In "Calculation Parameters", the % ENERGY LOSS is also displayed where the percentages that the plots and tables for the different energy losses are summarised.

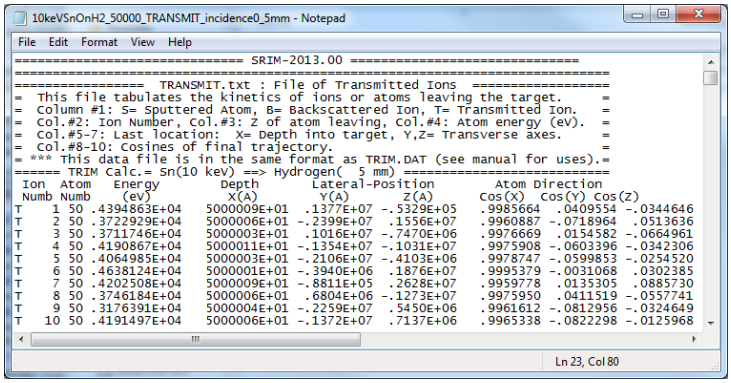

```
10keVSnOnH2_50000_TRANSMIT_incidence0_5mm - Notepad
File  Edit  Format  View  Help
============================ SRIM-2013.00 ============================
==============================================================================
================  TRANSMIT.txt : File of Transmitted Ions  =================
=  This file tabulates the kinetics of ions or atoms leaving the target.     =
=  Column #1: S= Sputtered Atom, B= Backscattered Ion, T= Transmitted Ion.   =
=  Col.#2: Ion Number, Col.#3: Z of atom leaving, Col.#4: Atom energy (eV).  =
=  Col.#5-7: Last location:  X= Depth into target, Y,Z= Transverse axes.     =
=  Col.#8-10: Cosines of final trajectory.                                   =
= *** This data file is in the same format as TRIM.DAT (see manual for uses).=
====== TRIM Calc.= Sn(10 keV) ==> Hydrogen(  5 mm) ========================
 Ion  Atom   Energy         Depth       Lateral-Position        Atom Direction
 Numb Numb    (eV)          X(A)         Y(A)       Z(A)      Cos(X)  Cos(Y) Cos(Z)
T    1 50 .4394863E+04   5000009E+01  .1377E+07 -.5329E+05   .9985664  .0409554 -.0344646
T    2 50 .3722929E+04   5000006E+01 -.2399E+07  .1556E+07   .9960887 -.0718964  .0513636
T    3 50 .3711746E+04   5000003E+01  .1016E+07 -.7470E+06   .9976669  .0154582 -.0664961
T    4 50 .4190867E+04   5000011E+01 -.1354E+07 -.1031E+07   .9975908 -.0603396 -.0342306
T    5 50 .4064985E+04   5000003E+01 -.2106E+07 -.4103E+06   .9978747 -.0599853 -.0254520
T    6 50 .4638124E+04   5000001E+01 -.3940E+06  .1876E+07   .9995379 -.0031068  .0302385
T    7 50 .4202508E+04   5000009E+01 -.8811E+05  .2628E+07   .9959778  .0135305  .0885730
T    8 50 .3746184E+04   5000006E+01  .6804E+06 -.1273E+07   .9975950  .0411519 -.0557741
T    9 50 .3176391E+04   5000004E+01 -.2259E+07  .5450E+06   .9961612 -.0812956 -.0324649
T   10 50 .4191497E+04   5000006E+01 -.1372E+07  .7137E+06   .9965338 -.0822298 -.0125968
Ln 23, Col 80
```

Figure 3.5: `TRANSMIT.txt` for 10 keV Sn ions in H_2 with a target depth of 5 mm. Column 1 gives the letter T for transmitted; column 2 - ion number; column 3 - atomic number of the ion; column 4 - energy of the transmitted ion (eV); column 5 - position on target depth axis when it was transmitted; column 6-7 - lateral position of the ion when it exits the target; column 8-10 - directional cosines of the trajectory of the transmitted ion. $\cos X$ is always positive since the x-axis measures the depth of the target; this is the scattering angle.

4 Results

The results below will focus on low velocity ions up to 10 keV (or 0.1 keV/u). First, a comparison of the different corrections used in SRIM is shown to further elaborate on the calculation of the stopping powers. Then, the straggling and projected ranges of the ions at the three above energies are tabulated. Next, the results of TRIM will be used to explore the different angle yields for ion energies of 0.1 keV, 1 keV, and 10 keV. Finally, the same simulation is implemented to analyse the energy spectrum of the transmitted ions for different outgoing angles as well as different target widths of H_2.

4.1 Stopping powers of Sn ions in H_2 with different corrections

As mentioned in section 2.3, there is a phase correction and compound correction for molecular hydrogen gas in SRIM. Four different stopping powers are compared in figure 4.1: molecular hydrogen solid with no compound correction, molecular hydrogen solid with Bragg's compound correction, molecular hydrogen gas with no compound correction, molecular hydrogen gas with Bragg's compound correction. The stopping powers of atomic hydrogen gas and solid were also compared to molecular hydrogen gas and solid, both with no compound correction, respectively. These were found to be equivalent making it redundant to add to the graphical representation of the deviations. The unit in use is independent of the density to allow for an accurate comparison between the different corrections.

Evidently, the corrections only affect the electronic stopping powers. Therefore, they do not have a critical effect on the total stopping powers in low velocities as the electronic stopping power is a small fraction of the total stopping power. Assuming that molecular hydrogen gas with Bragg's compound correction is the accepted value, the percentage error compared to the accepted value of the total stopping power, projected range, longitudinal straggling and lateral straggling is 3.00%, 4.02%, 5.64% and 5.85%, respectively.

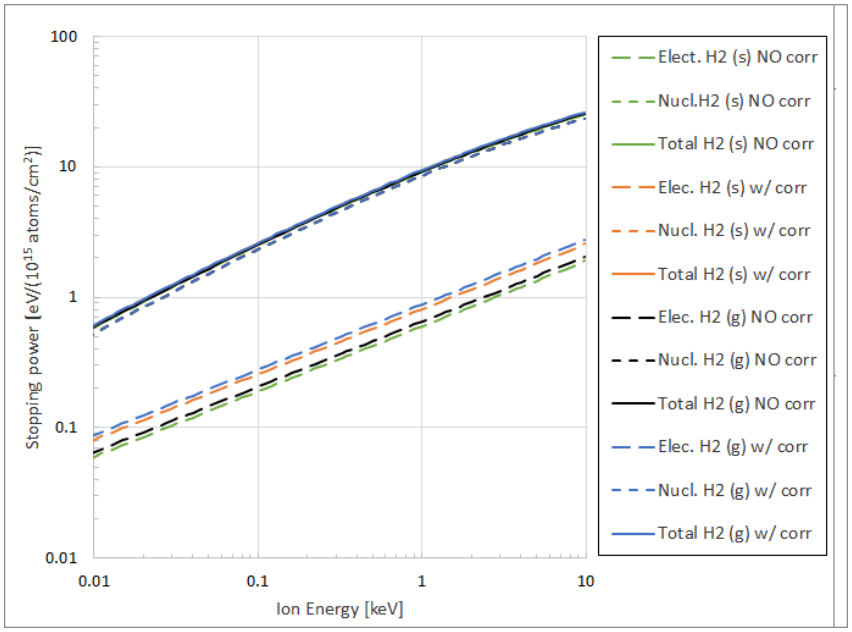

Figure 4.1: A graph depicting the different stopping powers for hydrogen gas and solid with and without the corrections on SRIM. By comparing the phase correction to the compound correction, it is clear that there is a greater deviation in the compound correction. Both corrections only affect the electronic stopping while the nuclear stopping is the exact same for all the simulations. Note that the nuclear stopping powers overlap. Since the electronic stopping power is a negligible portion of the total stopping power, the difference in the different hydrogen targets from the electronic stopping power is not visible in the total stopping power.

Table 2: The numerical minimum and maximum value for the different total stopping powers at 10 keV. The maximum total stopping power corresponded to that of H_2 in the gas phase with Bragg's compound correction which also gave the minimum straggling and range; this is to be the true value of the stopping power with the least deviation from the experimental results. The minimum total stopping power corresponded to that of H_2 in the solid phase with NO compound correction.

	total energy [eV/(10^{15}atoms/cm^2)]	projected range [µm]	longitudinal straggling [µm]	lateral straggling [µm]
max	26.21	13960	928.42	651.15
min	25.43	13420	878.88	615.17
difference	0.78	540	49.54	35.98

4.2 Projected range and straggling of different Sn ions energies in H_2 gas

To confirm the proportionality of density with the projected ranges of ions in matter, the straggling and range has been summarised in table 3 for the default density at STP and for the lowest attainable density through SRIM before it rounds down to zero. All values were obtained by running TRIM for 20,000 Sn ions in H_2 with a target depth of 2 cm. In general, with decreasing energy, the range decreases. This is reflected by equation 14 which shows the direct relation between ion's velocity (or energy) and range straggling.

Table 3: The range and straggle of 10 keV, 1 keV and 0.1 keV Sn projectiles in H_2 gas. For the three tables on the left, $\rho = 8.9 \times 10^{-7}\,\mathrm{g\,cm^{-3}}$ and on the right, $\rho = 8.9 \times 10^{-5}\,\mathrm{g\,cm^{-3}}$. Evidently, the range and straggle are directly proportional to the density. Furthermore, with decreasing Sn projectile energy, the range and straggle of the ions decreases.

$\rho = 8.9 \times 10^{-7}\,\mathrm{g\,cm^{-3}}$

	longitudinal	lateral proj	radial
10 keV range	14.1 mm	519 µm	813 µm
10 keV straggle	617 µm	651 µm	427 µm
1 keV range	4.97 mm	178 µm	280 µm
1 keV straggle	165 µm	223 µm	145 µm
0.1 keV range	1.95 mm	58.7 µm	92.7 µm
0.1 keV straggle	55.8 µm	73.7 µm	48.5 µm

at STP, $\rho = 8.9 \times 10^{-5}\,\mathrm{g\,cm^{-3}}$

	longitudinal	lateral proj	radial
10 keV range	141 µm	5.17 µm	8.14 µm
10 keV straggle	6.17 µm	6.49 µm	4.27 µm
1 keV range	49.7 mm	1.78 µm	2.8 µm
1 keV straggle	1.66 µm	2.23 µm	1.46 µm
0.1 keV range	19.5 µm	589 nm	931 nm
0.1 keV straggle	555 nm	739 nm	488 nm

Furthermore, a relation was found between the ranges and the ion energy through least squares fitting to find the power rule to produce the best correlation. This is presented in figure 4.2 for the projected range and figure 4.3 for the range straggling in the longitudinal and lateral planes.

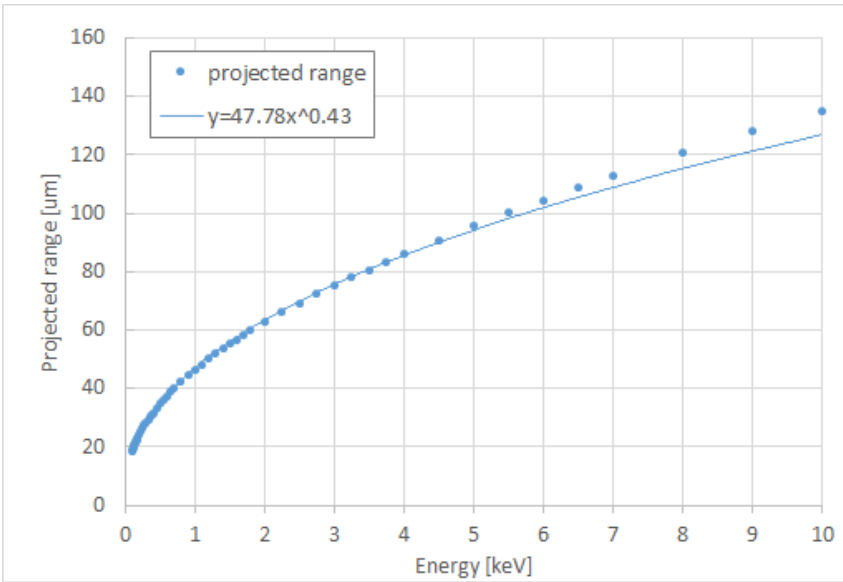

Figure 4.2: A graph showing the projected range as calculated by SRIM for tin ion energies 0.1 keV–10 keV in hydrogen gas target. The power rule derived for the entire range is $\bar{R}_p(E) = 47.78E^{0.43}$ with a correlation coefficient $R^2 = 0.9985$. This correlation increases to 0.9992 when taking the energy up to 5 keV and 0.9999 when taking the energy 5 keV–10 keV. The relation clearly changes for the different energy ranges.

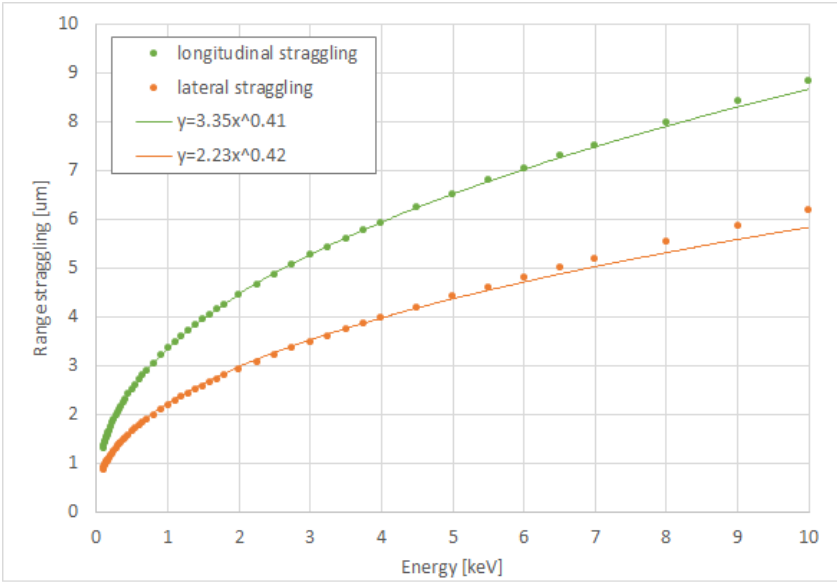

Figure 4.3: A graph showing the longitudinal range straggling and lateral range straggling as calculated by SRIM for tin ion energies 0.1 keV–10 keV in hydrogen gas target. The power rule derived for the entire range is $\sigma_x(E) = 3.35E^{0.41}$ with a correlation coefficient $R^2 = 0.9999$ and $\sigma_y(E) = 2.23E^{0.42}$ with a correlation coefficient $R^2 = 0.9987$ for longitudinal and lateral straggling, respectively. This correlation increases to 1 and 0.9994 when taking the energy up to 5 keV; 0.9997 and 0.9999 when taking the energy 5 keV–10 keV. The relation clearly changes for the different energy ranges.

4.3 Energy spectrum of the transmitted Sn ions

As thicker target widths allow for more collisions, Sn ions trajectories leave the target with a deviation in the angle of the transmitted ion. All simulations from here on out were done for 20,000 ions at an incidence angle of 0°. To understand how the energy spectrum of the transmitted ions differs for target depths, several graphs were plotted. First, figure 4.4, where the trend of the energy spectrum is shown for increasing widths from 1 mm to 12 mm. The angle out range was taken from 0° up to the angle with the maximum yield of the largest width. This was found to be 5° for 10 keV. Second, figure, to show the energy loss of transmitted ions with smaller target depths of 1 µm, 10 µm and 100 µm compared to larger target depths of 1 mm and 10 mm. Both these plots were replicated for 1 keV and 0.1 keV; however, with different target depths as lower energies give a smaller range as shown in table 3. The energy was taken in steps of 20 eV for 10 keV and 1 keV; and in steps of 2 eV for 0.1 keV.

The number of transmitted ions that left the target at an angle of $0 \pm 5°$ decreased with increasing width as there was a larger scattering angle due to an increased number of collisions. For example, the number of transmitted ions following within the range of 0° to 5° is 19,996 ions for 1 mm whereas for 12 mm it is only 7,656 ions. Yet, the peak of the curve increases for smaller target depths; this is because the energy spectrum also gets narrower. The shift in the energy spectrum is evident as the energy of the transmitted ions nears zero as it approaches the stopping range of 14 mm as shown in table 3. Nonetheless, the energy spectrum is more or less symmetrical about the peak until the peak gets close to zero for 10 mm.

A similar evaluation was done for ion energies of 1 keV and 0.1 keV (shown in figure 4.5) but for fewer widths. The trend proved to be consistent for the different ion energies. This is especially true for the energy spectrum of 1 keV as the peak is extremely narrow for 4 mm and 100 µm at both ends of the plot.

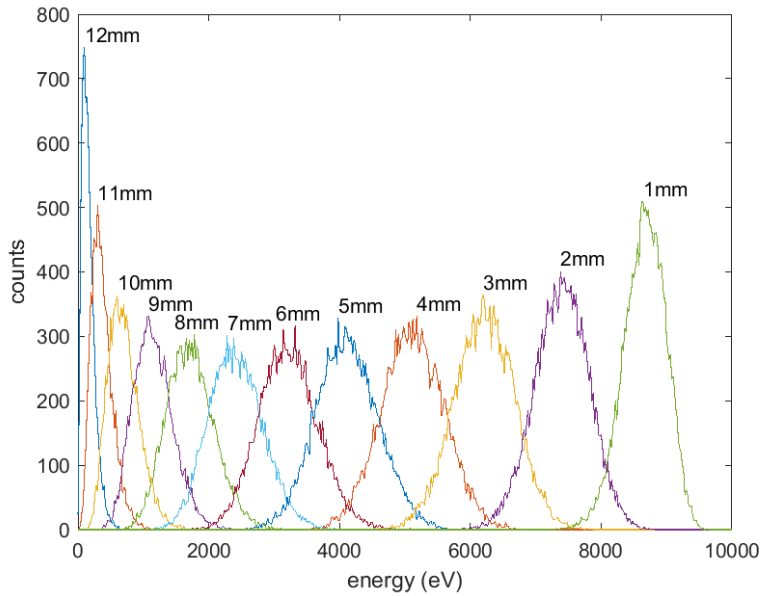

Figure 4.4: The energy spectrum for 10 keV tin ion going through hydrogen gas target with an outgoing angle of 0° to 5°. Each curve represents a different target depth ranging from 1 mm to 12 mm.

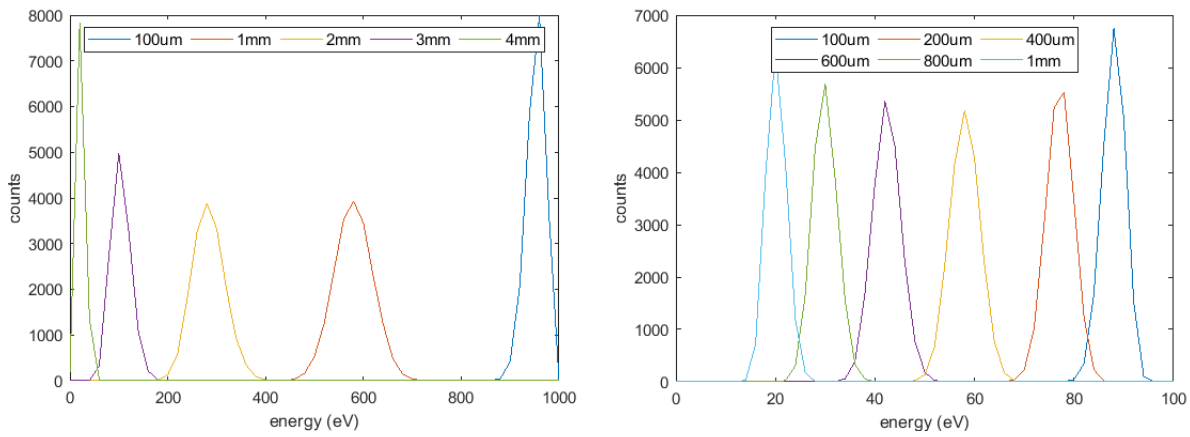

Figure 4.5: On the left, the energy spectrum for 1 keV and on the right, the energy spectrum for 0.1 keV of different widths for an outgoing angle of 0° to 5°. The peaks are sharper due to a relatively larger energy step compared to that of 10 keV in figure 4.4. For 0.1 keV, the trend is less obvious since almost all of the transmitted ions fall within the angle range.

10keV

Continuing the analysis of the above data, for 10 keV, over 90% of the transmitted ions lose no energy when passing through thin target depths. At a width of 1 µm, only 292 out of 20,000 ions lose up to 320 eV energy. At 10× that width, 3,216 out of 20,000 ions lose up to 420 eV of their energy, making around a 10% increase in the number of ions that lose energy. Even for a width of 100 µm, there were a few counts at 10 keV as shown below in figure 4.6.

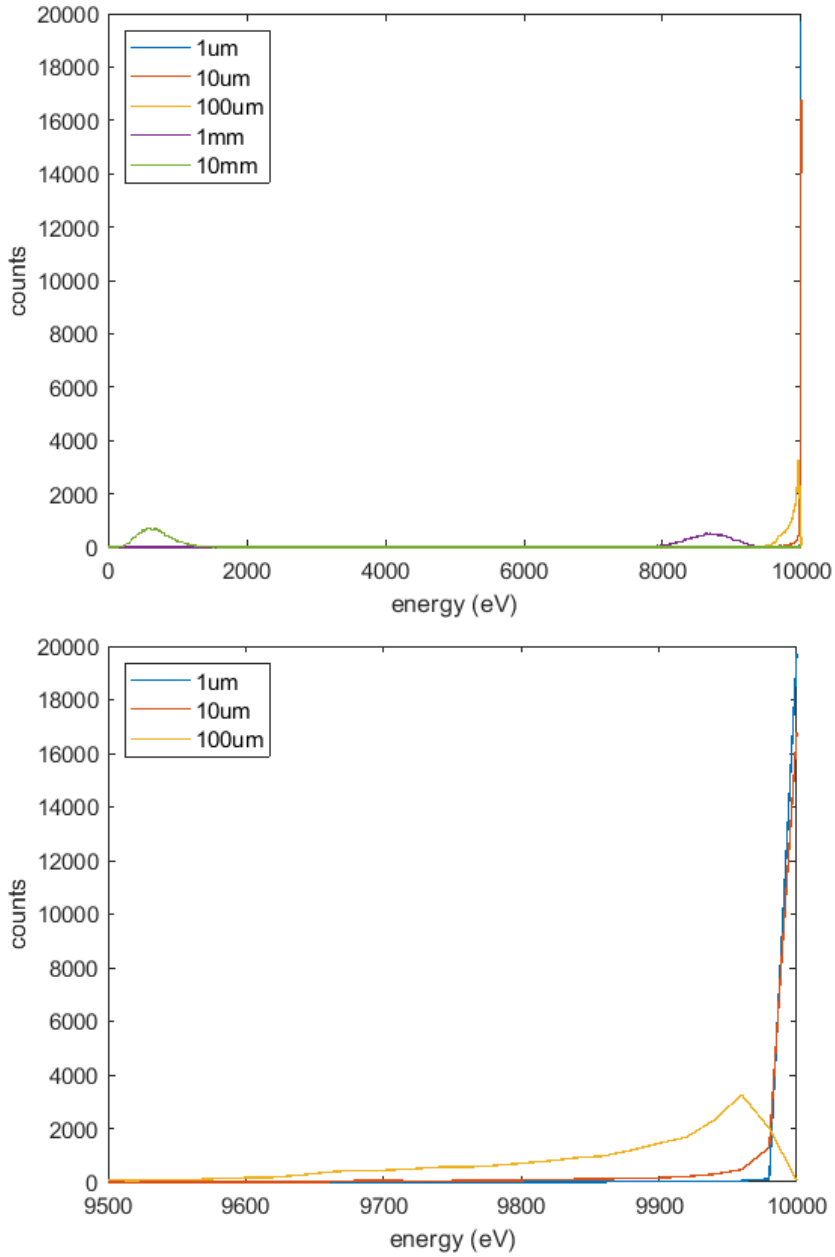

Figure 4.6: A graphical display of the energy loss of 10 keV at a width of 1 µm, 10 µm, 100 µm, 1 mm and 10 mm with a deviation angle of 0°-5°. At the top of the page, the full energy spectrum while below it, an enlargement of the plot including only the smaller target depths is displayed to see the energy loss more clearly.

1keV

For 1 keV at a width of 1 µm, only 334 out of 20,000 ions lose up to 40 eV energy. At 10× that width, 3,431 out of 20,000 ions lose up to 80 eV of their energy, making around a 15% increase in the number of ions that lose energy. Albeit less, for a width of 100 µm there were a few counts at 1 keV as well. It seems that more ions lose energy; however, this could be because of the relatively large energy steps which were kept constant to that of 10 keV for better comparison. The same data was plotted with energy steps of 5 eV to see if that is the case. However, as shown in table 4, this turned out to be false.

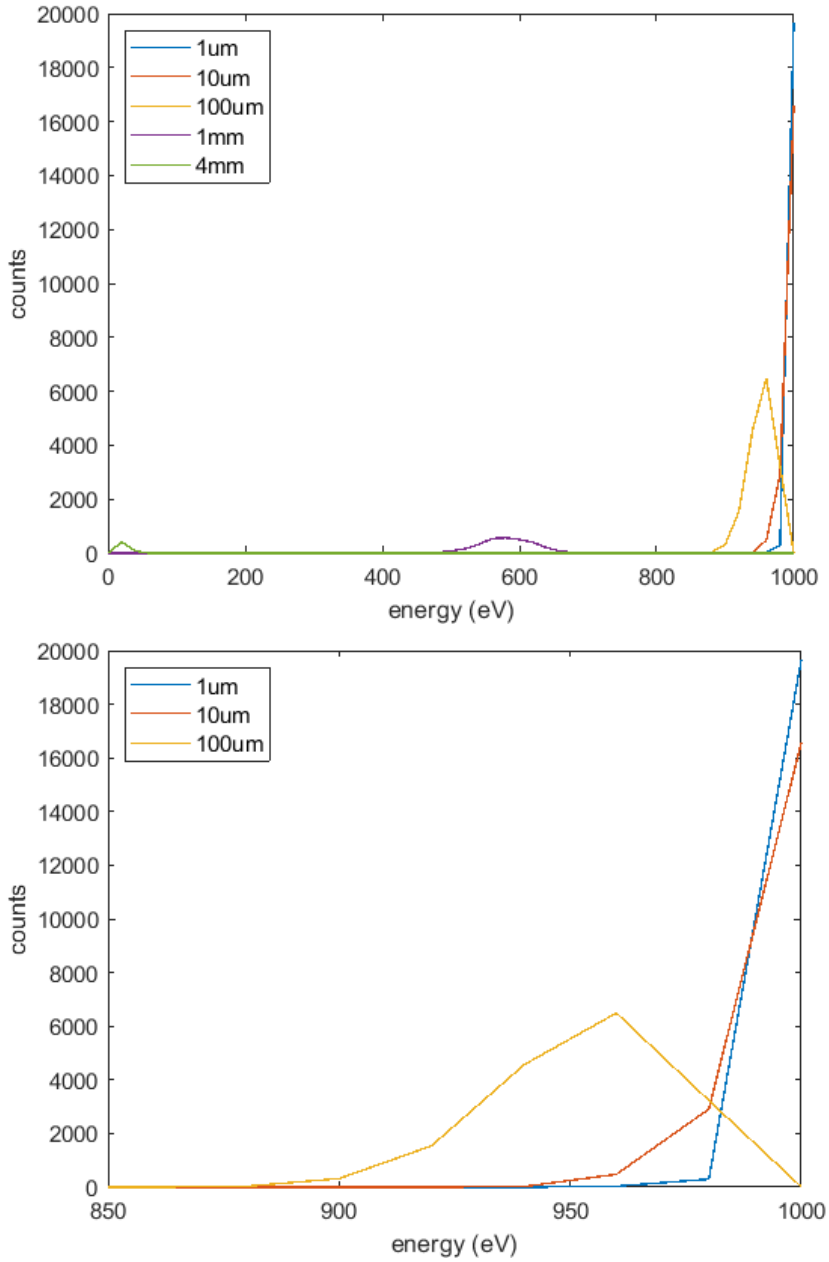

Figure 4.7: A graphical display of the energy loss of 1 keV at a width of 1 µm, 10 µm, 100 µm, 1 mm, 2 mm, 3 mm and 4 mm with a deviation angle of 0°-5°. At the top of the page, the full energy spectrum while below it, an enlargement of the plot including only the smaller target depths is displayed to see the energy loss more clearly.

Table 4: A tabulated presentation of the number of ions that lose energy when transmitted through different target widths. Also, showing the maximum energy lost after transmission. The counts increase for smaller energy steps as it evaluates more ions with $E_{lost} < 5\,\text{eV}$ which is not shown in the data for larger energy steps. Furthermore, at a target depth of 100 µm, all ions transmitted lose at least 2.5 eV of energy to the target which is displayed in the data for Estep = 5 eV but not in Estep = 20 eV as 10 of the ions lose less than 10 eV.

Target depth	Counts (Estep = 20 eV)	Max E_{lost} [eV]	Counts (Estep = 5 eV)	Max E_{lost} [eV]
1 µm	334	40	716	35
10 µm	3,431	80	7,029	70
100 µm	19,990	140	20,000	135

0.1keV

The energy steps were changed to 2 eV for 0.1 keV since it is in a very low energy range. Unlike the results of 1 keV and 10 keV, there were no ions leaving a target depth of 100 µm without energy loss. Furthermore, 911 out of 20,000 transmitted ions lost energy for a depth of 1 µm with a maximum loss of 8 eV; while 9,534 out of 20,000 transmitted ions lost a maximum of 6 eV when transmitted through a depth of 10 µm. This means that almost half of the transmitted ions loss some of their energy when going through a target depth of 10 µm or more.

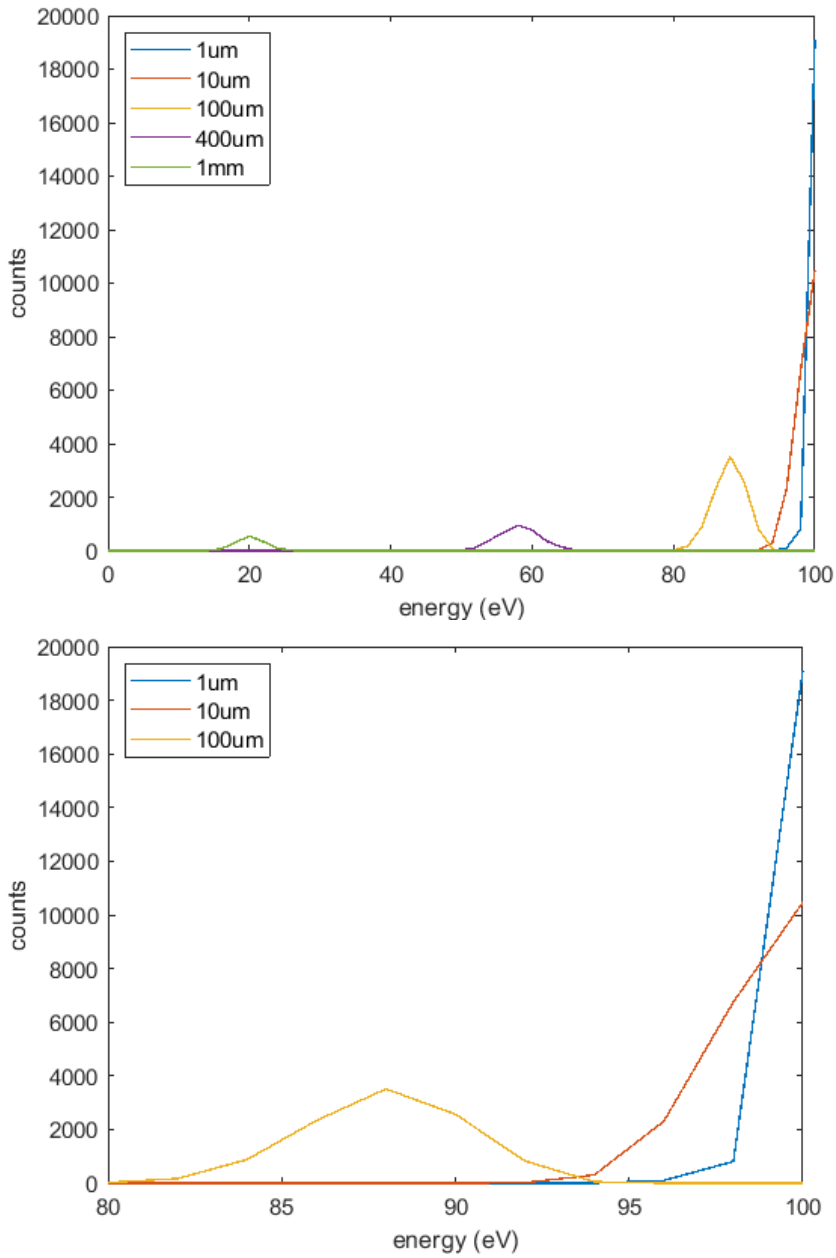

Figure 4.8: A graphical display of the energy loss of 0.1 keV at a width of 1 µm, 10 µm, 100 µm, 400 µm and 1 mm with a deviation angle of 0°-5°. At the top of the page, the full energy spectrum while below it, an enlargement of the plot including only the smaller target depths is displayed to see the energy loss more clearly.

4.4 Angle yields of different H_2 target depths

In accordance with Rutherford's scattering law in equation 10, the scattering angle strongly depends on the target depth and ion energy. This is clearly depicted in figure 4.9 for two different target depths. The deviation from the incidence angle increases with decreasing energies as the ions move slower allowing for further stopping.

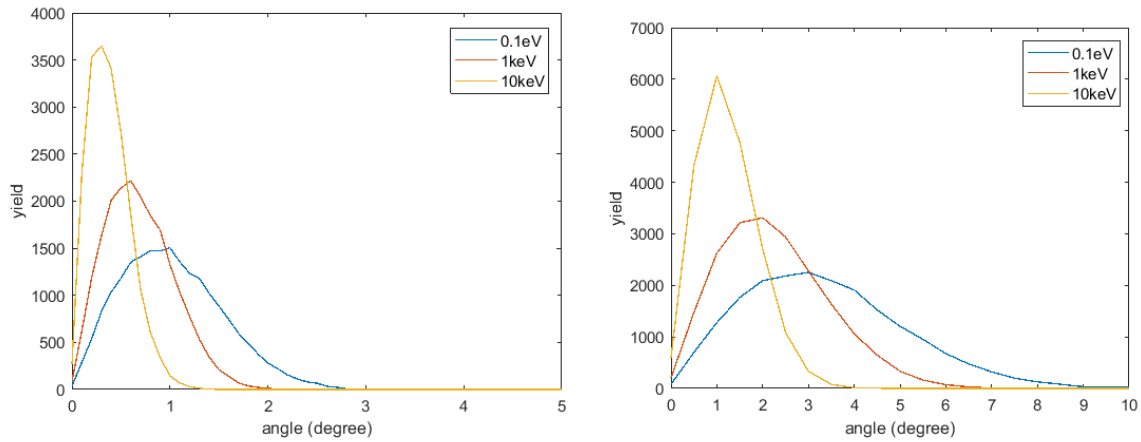

Figure 4.9: Two plots of the angle yield for 0.1 keV, 1 keV and 10 keV for a target depth of 100 µm and 1 mm. The intervals are taken by 0.1° and 0.5°, respectively. The increase in scattering angle is evident when comparing the curves of the lower energies to that of higher energies.

Since this thesis's main focus is the transmission of ions in a target depth of 1 µm, this is shown separately in figure 4.10 to be compared to the plots in figure 4.9. Despite the sharp spike at an angle less than 0.05°, the trend that was shown in figure 4.9 can still be seen; the number of ions that exit the target with a very small scattering angle decreases for lower energies.

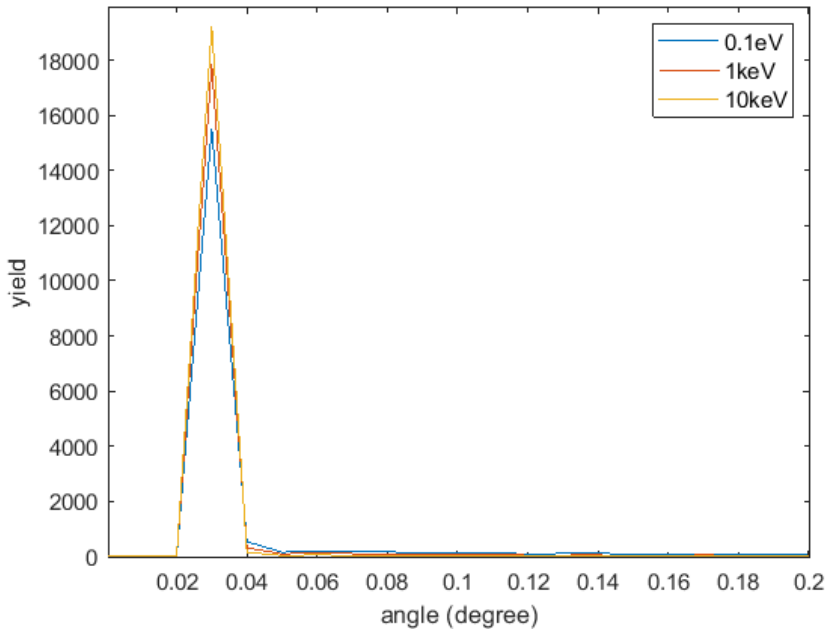

Figure 4.10: A plot for the angle yield of 0.1 keV, 1 keV and 10 keV transmitted ions for a target depth of 1 µm. The intervals are taken by 0.01°; however, it is still difficult to observe the change in the angle yield as the target depth is so small that the scattering angle is very close to 0°.

4.5 Energy spectrum of different angle yields

Now that the angle yield is understood, it is possible to dive into the energy spectrum for the different energies and their corresponding scattering angles. Figure 4.11 shows the yield of transmitted ions with different scattering angles.

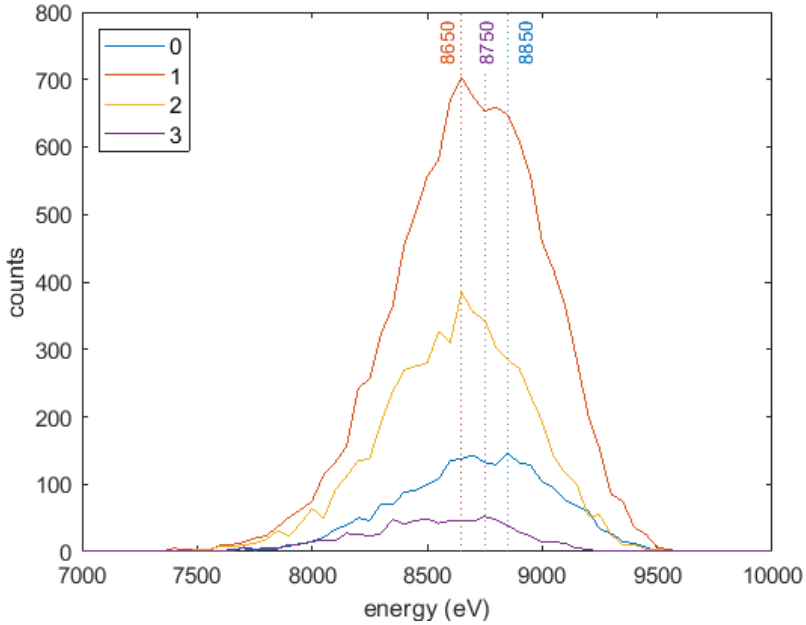

Figure 4.11: The energy spectrum for 10 keV Sn ions in H_2 gas with a target width of 1 mm transmitting ions with a scattering angle of 0° to 3° enlarged to investigate any differences in their energy spectrum. Each angle was given with an error margin of 0.5°. The transmitted ion energy with most counts has been indicated with a dotted line. Note that the lines for 1° and 2° overlap.

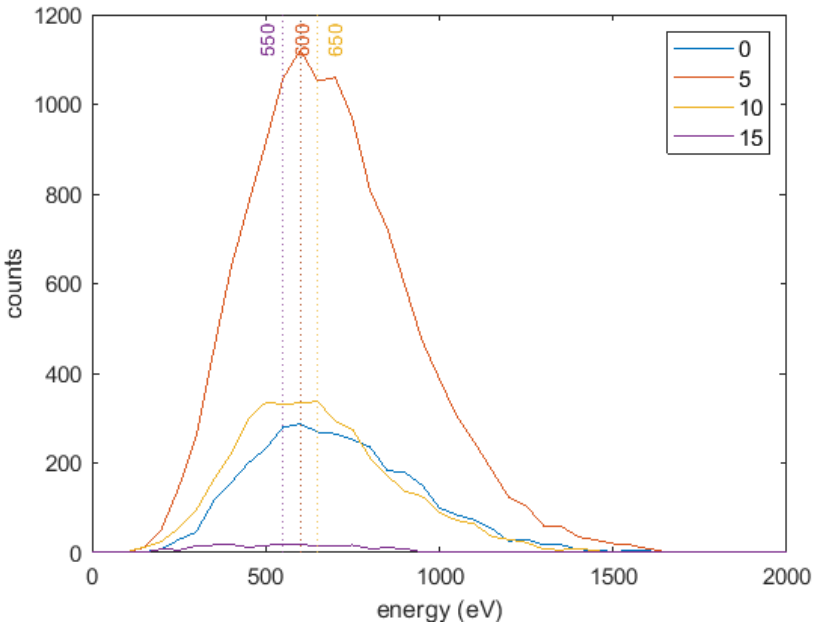

Figure 4.12: The energy spectrum for 10 keV Sn ions with a target width of 10 mm transmitting ions with a scattering angle of 0° to 15° enlarged to investigate any differences in their energy spectrum. Each angle was given with an error margin of 2.5°. The transmitted ion energy with most counts has been indicated with a dotted line. Note that the lines for 0° and 5° overlap.

Although the shift in the energy spectrum is not large, it should be noted. The largest difference is between 0° and 1°/2°. This is because the margin is ±0.5; however, there is no scattering angle lower than 0° making the angle range smallest for 0°. This will be further discussed in section 5.4. The difference in the energy with the maximum counts is less than 500 eV. The same follows for figure 4.12.

5 Discussion

The largest limitation faced when using SRIM was the lack of experimental data available to compare the transmission of heavy ions in light gas targets with the simulated results. Furthermore, the target particles are taken to be static at all times at STP conditions. In reality, the hydrogen gas is under a constant high flow under very low pressure. Only a comparison with experimental results would prove that a simulation for tin ion in hydrogen gas with density $\rho = 8.89 \times 10^{-7}\,\mathrm{g\,cm^{-3}}$ and depth 1 µm at standard temperature and pressure gives similar results to that of hydrogen gas with standard density $\rho = 8.89 \times 10^{-5}\,\mathrm{g\,cm^{-3}}$ and depth 1 cm at a pressure 10×10^{-5} mbar as used in the laboratory.

In addition, many interactions are not taken into account in the program. These include the multiple scattering effect and the change in the projectile ion and target atom's charge state after electron capture. When an ion of a few keV interacts with matter, electron capture occurs which reduces the effective charge. The multiple scattering effect is a consequence of many different defects between the electrons in the ion and the atoms in the target. This can vastly alter any results obtained through SRIM as will be discussed further below. Overall, available data shows an average error of 2% with some exceptions going as high as 5% [6].

5.1 Stopping powers of Sn ions in H_2 with different corrections

Despite choosing a unit independent of density (eV/(10^{15}atoms/cm^2)), there were evident discrepancies between the stopping powers of tin ion in hydrogen. The primary parameter for stopping powers is the ion velocity. As this thesis focuses on the low ion velocity region of about 1 keV/u, the corrections have little ramifications on the stopping power. The only effect the corrections have on the stopping power lie in the electronic stopping. Afterall, nuclear stopping energy is calculated through the interaction between particles' nuclei which is identical for all hydrogen atoms, whereas, electronic stopping energy relies on the inelastic collisions between bound electrons in the target and the ion moving through it. This is dependent on the chemical bond created between different hydrogen atoms and tin ions and changes for different structures of the target. Due to the compound and phase corrections explained in section 2.3, molecular hydrogen gas has the largest stopping power as it induces the most collisions with tin ions.

It should also be noted that previous experimental data conceived by a group of scientists [20], gave a discrepancy between the electronic stopping power calculated using the LSS theory and that given by SRIM. The reason for this was unclear but it may have likely been due to the estimate of the charge state run by SRIM. From the paper, it can be assumed that SRIM overestimates the electronic stopping power as it did for heavy ions just like it was shown for Si, but this is not definite.

As previously stated, SRIM's theoretical physics background on heavy ions in light targets has not been backed up by enough experimental data to make it a governing theory for all heavy ions in the low energy region. This adds to the lack of precision in the results found for the stopping powers. However, as the total stopping power for molecular hydrogen gas is largest as was expected, these results can be

conclusive.

5.2 Comparison of stopping with experimental data

Experimental results of the stopping power of hydrogen gas on Sn^+ and Sn^{2+} ions have been measured within the same range (0.1 keV–10 keV) by previous studies [5]. Using the measured time of flight, the stopping cross-section for a given ion energy was calculated. It was found that the least squares fitting resulted in the approximation of $S = 1.59E^{0.7}$ for Sn^+ ions and $S = 1.46E^{0.54}$ for Sn^{2+} ions, where S is the stopping cross-section and E is the ion energy. From this it follows that the best fit for Sn^{2+} ions is nearly proportional to the ion velocity.

In contrast, using the same method of approximation, $S = 0.902E^{0.508}$ from figure 2.3 with a correlation coefficient $R^2 = 0.997$ within in the range of 0.1 keV–10 keV; and $S = 0.916E^{0.525}$ with a correlation coefficient $R^2 = 0.998$ showing an even stronger power rule. Clearly, there is a large difference between the experimental value and the simulated value found for the stopping cross-section. The most significant difference between the two input parameters lies within the ion charge state. Furthermore, the experimental data was obtained through a varying pressure gradient giving a varying density whereas SRIM runs for a constant gas density. Following Firsov's model and the nuclear stopping theory, the stopping is proportional to the atomic radius [12]. Consequently, the lower stopping cross-section found through SRIM shows that the ionic radius is very small as a result of neutral charge.

5.3 Straggle and projected ranges of different Sn ions energies

Table 3 proves the direct proportionality between the density of the target and the produced straggle and range of the projected ions. Since many interactions are not considered in SRIM, these values are likely to be overestimates of the experimental values. More collisions would further increase the stopping powers, consequently decreasing the straggle and projected ranges. Although the ion energies are reduced by an order of magnitude, the straggle and range decreased at a slower rate.

Similarly to the relation explained in section 5.2, the relation found in figures 4.2 and 2.4, provides a strong correlation between the projected range/straggling and the energy when using the least square fitting with the power rule. There is also a clear indication that the power rule constants change for larger ranges $>\sim 5$ keV. However, there is no experimental data to compare the simulation results to.

The experimental studies done for straggling is even less than that of stopping powers, hence the increased inaccuracies in the values that result from the theories behind SRIM's calculations. Yet, it seems that the range straggling is not linearly related to the ion velocity as predicted by equation 14 but the general relation could hold true.

5.4 Angle yield and energy spectrum of different Sn ions energies and H_2 target widths

The general consensus is that as the target depth increases, more energy is lost by the projectile ions to the target atoms and the scattering angle range increases. At small target depths 1 µm only about 1.46% of 10 keV, 1.67% of 1 keV, and 4.55% of 0.1 keV tin ions lost any energy to hydrogen molecules.

The most crucial variable not taken into account when plotting the energy spectrum and angle yield for different angles is the area that the transmitted ions exit the target with. When an ion leaves the target with a scattering angle, the script is run for that angle in all lateral directions; hence, producing a cone-like structure. All ions within that cone are counted and plotted meaning that more ions are

captured within a cone for a larger angle than a smaller angle. As a result, the yield for 0° is often underestimated.

Interestingly, there were shifts in the energy spectrum for discrete scattering angles as shown in figure 4.11 and figure 4.12. Although small, it is still to be considered. This could be due to the reason stated above resulting in inaccurate counts of transmitted ions at certain energies.

6 Conclusion

As was expected, transmitted tin ions lose more energy in larger target depths. The exact counts and energy spectrum depend on the target depth. However, it was assumed that the scattering angle would not diverge much. The above research found that there are large deviations for target depths over a few micrometers for all ion energies. Furthermore, the different angles presented a marginal energy shift that could be of importance under different conditions. None of the above results can be entirely conclusive as SRIM simulations contain several uncertainties which are difficult to be considered quantitatively with the limited experimental data available. Moreover, the simulations were run under STP conditions and EUV devices use a heavy flow of hydrogen gas under lower pressures.

The purpose of this research was to investigate the results of the simulations for future experimental comparisons to be made with. Proper experiments are required to study the stopping powers of hydrogen gas in low pressure which can then be compared to the above results. This will be vital to assess the ideal target depth needed for hydrogen gas to stop the tin ions from damaging the focusing mirrors installed in ASML's EUV lithography device.

Acknowledgements

Despite the difficult times during this pandemic, this research group pulled me through the days with insightful discussions and consistent virtual meetings. First and foremost, I am grateful to Ronnie Hoekstra for finding an alternative to my planned experimental research. I owe most of my graphical outputs to Klaas Bijlsma for his codes in MatLAB and effort to explain it to me, making these diagrams would not have been possible without him. I would also like to thank Subam Rai for his input during the meetings and noticing any missing content. It would have been all the better had I been able to work under his supervision in a lab. Furthermore, I would like to thank Thomas Schlathölter for his time when reading this report. Many thanks to the Gas Target group for the motivation by sharing what they had done every week. Lastly, I want to thank the members of the QISD group for the coffee hours through Zoom. Hopefully, when it is possible, we can all meet in real life and grab an actual cup of coffee together!

References

[1] "Over 50 years of moore's law." [Online]. Available: https://www.intel.com/content/www/us/en/silicon-innovations/moores-law-technology.html

[2] "ASML EUV lithography systems." [Online]. Available: https://www.asml.com/en/products/euv-lithography-systems

[3] M. J. Deuzeman, "Generation and interaction of energetic tin ions," PhD thesis, University of Groningen, 2019.

[4] S. Harilal, B. O'shay, Y. Tao, and M. Tillack, "Ion debris mitigation from tin plasma using ambient gas, magnetic field and combined effects," *Applied Physics B*, vol. 86, no. 3, pp. 547–553, 2007.

[5] D. B. Abramenko, M. V. Spiridonov, P. V. Krainov *et al.*, "Measurements of hydrogen gas stopping efficiency for tin ions from laser-produced plasma," *Applied Physics Letters*, vol. 112, no. 16, p. 164102, Apr. 2018. [Online]. Available: https://doi.org/10.1063/1.5025914

[6] J. B. J.F. Ziegler and M. Ziegler, *SRIM - The Stopping and Range of Ions in Matter.* SRIM Co., 2008.

[7] W. P. P. S. H. V. R. Behrisch, W. Heiland, "Ion surface interaction, sputtering and related phenomena." *Kristall und Technik*, vol. 9, no. 12, pp. K113–K114, 1973. [Online]. Available: https://onlinelibrary.wiley.com/doi/abs/10.1002/crat.19740091215

[8] M. Kokkoris, "Joint ICTP-IAEA workshop on nuclear reaction data for advanced reactor technologies," 2013.

[9] P. Van der Heide, *Secondary ion mass spectrometry: an introduction to principles and practices.* John Wiley & Sons, 2014.

[10] S. P. A. Sauer, J. Oddershede, and J. Sabin, *Theory and Calculation of Stopping Cross Sections of Nucleobases for Swift Ions*, 11 2012, pp. 191–200.

[11] J. Lindhard, M. Scharff, and H. E. Schiøtt, *Range concepts and heavy ion ranges.* Munksgaard Copenhagen, 1963.

[12] E. Rutherford, "Lxxix. the scattering of α and β particles by matter and the structure of the atom," *The London, Edinburgh, and Dublin Philosophical Magazine and Journal of Science*, vol. 21, no. 125, pp. 669–688, 1911.

[13] M. Backman, "Effects of nuclear and electronic stopping power on ion irradiation of silicon-based compounds," dissertation, University of Helsinki, 2012.

[14] O. Tjepkema, "The missing single-scattering peak in low-energy heavy ion scattering off surfaces," July 2019.

[15] N. Bohr, *The penetration of atomic particles through matter.* Munksgaard Copenhagen, 1948.

[16] W. Wilson, L. Haggmark, and J. Biersack, "Calculations of nuclear stopping, ranges, and straggling in the low-energy region," *Physical Review B*, vol. 15, no. 5, p. 2458, 1977.

[17] J. P. Biersack and L. Haggmark, "A monte carlo computer program for the transport of energetic ions in amorphous targets," *Nuclear Instruments and Methods*, vol. 174, no. 1-2, pp. 257–269, 1980.

[18] D. Thwaites, "Bragg's rule of stopping power additivity: A compilation and summary of results," *Radiation Research*, vol. 95, no. 3, pp. 495–518, 1983.

[19] J. R. Sabin and J. Oddershede, "Theoretical stopping cross sections of c-h, c-c and c= c bonds for swift protons," *Nuclear Instruments and Methods in Physics Research Section B: Beam Interactions with Materials and Atoms*, vol. 27, no. 2, pp. 280–286, 1987.

[20] A. Mangiarotti, M. Lopes, M. Benabderrahmane *et al.*, "A survey of energy loss calculations for heavy ions between 1 and 100 kev," *Nuclear Instruments and Methods in Physics Research Section A: Accelerators, Spectrometers, Detectors and Associated Equipment*, vol. 580, no. 1, pp. 114–117, 2007.